Parabolic Deformable Mirror Project Development and Device Characterization

Tyler D. Groff[a], Hari B. Subedi[a], Evan Bray[a,b], Guangjun Gao[a], Neil T. Zimmerman[a], Michael W. McElwain[a]
[a]NASA Goddard Space Flight Center, Greenbelt, MD
[b]Peraton, Greenbelt, MD 20771

Abstract.
Existing state-of-the-art wavefront sensing and control setups for the imaging of exoplanets utilize two high-actuator count flat deformable mirrors (DMs) to control both phase and amplitude aberrations. One of the objectives of the Exoplanet Spectroscopy (ExoSpec) project at Goddard Space Flight Center (GSFC) is to improve upon this regime through the development of parabolic deformable mirrors (PDMs), which can address several of the key limitations in existing setups. Specifically, the need for flat DMs to be located in conjugate pupil planes drives unique packaging challenges that can be overcome by allowing the off-axis imaging elements to be controllable as well. In addition, simulations show that the use of deformable powered elements will increase the overall controllable bandwidth, up to 35% over 5-12 λ/D. To pursue this effort, the ExoSpec group has begun testing a first-generation parabolic DM, which is already informing a second generation design. This paper will provide a comprehensive update on its characterization, including influence function measurements, linearity analysis, closed-loop wavefront control performance, and thermal stability assessment.

Keywords: Deformable mirror, parabolic deformable mirror, HWO, wavefront sensing and control, exoplanets.

1 Introduction

Coronagraph instruments exhibit inherent sensitivity to optical aberrations, as these aberrations generate quasi-static speckle patterns within the high-contrast dark zones imaged by the science camera. These speckle patterns are corrected with deformable mirrors (DMs). The conventional solution is to use two high-actuator density DMs, taking advantage of mixing between phase and amplitude of the electric field as the light propagates between them for controllability of both amplitude and phase aberrations.[1,2] In contrast, by placing the actuators at the existing optical surfaces of the instrument means the correction is closer to a conjugate plane where the aberrations occur. With a more direct compensation of the aberrations in the instrument, this configuration is less reliant on a more complex interaction of phase-induced amplitude aberrations compared to the two DMs in series. One advantage of this is the potential to have a more graceful degradation in contrast as the optical bandwidth increases, which ultimately can improve the efficiency of spectroscopic characterization of exoplanets. Using this guiding principle, Groff et al.[3] examined the effectiveness of utilizing lower actuator density configurations across multiple optically conjugate surfaces to supplement a single high actuator density DM positioned at the pupil. These controllable imaging elements, commonly off-axis parabolas in a coronagraph instrument, are coined parabolic deformable mirrors (PDM) though the prescription is fundamentally controllable. It is interesting to consider the architecture of a high-order pupil DM paired with PDMs and how they interact with the telescope aberrations. The in-pupil DM, being optically conjugate to the primary mirror, will provide most of the control authority against phase aberrations and the PDMs largely handle amplitude control. Having control authority at more optical planes will be advantageous to improving the optical bandwidth of the correction.

In addition to the wavefront control advantages, the PDM implementation presents some systems-level advantages. Controlling at multiple surfaces will realize some trades in instrument layout complexity, but fewer overall actuators likely results in a net risk reduction (particularly when considering harnessing and drive electronics). This has the potential to realize significant mass and power savings. Eliminating the requirement for a far out-of-pupil DM also simplifies packaging. The very large propagation distance required between the two DMs significantly constrains instrument volume. With simulations supporting improved optical bandwidth and little to no penalty in the achievable contrast, PDMs are a compelling option for instrument trade studies within the Habitable Worlds Observatory (HWO) architecture. It is worth noting that the PDM affords the opportunity to reduce the number of reflections. This is likely a modest improvement in visible or near-infared coronagraphs, but is potentially very enabling as a single DM in an ultraviolet instrument where surface reflections come at much greater cost in throughput.

Development of the PDM has been funded through the Exoplanet Spectroscopy Technologies (ExoSpec) project, which consists of four different principal task areas (spectral retrieval, detectors, integral field spectroscopy, and PDMs) at NASA Goddard Spaceflight Center (GSFC). The overall objective of the project is to advance the technology readiness level (TRL) of key enabling technologies and spectroscopic retrieval and detection methods, aiming to optimize exoplanet spectroscopic capabilities for the upcoming HWO.

Here we begin with coronagraph simulations that motivate the use case of the PDM in Section 2, and describe the high-level development plan to-date in Section 3. An overview of the PDM design constraints and the resultant specifications of the first generation (Gen1) prototype is described in Section 4, followed by the characterization work we have completed thus far in Section 5. These results cover influence functions and linearity, "flattening" the PDM wavefront with closed-loop control, and actuator response to thermal variations. We finish with future development plans and conclusions based on testing of the Gen1 in Sections 6 and 7.

2 Coronagraph Simulations with PDMs

Looking back to Groff et al .,[3] the first simulations used a shaped pupil coronagraph (SPC) "ripple 3" design[4] to perform trade studies to determine the efficacy of using PDMs for wavefront control. The ripple 3 design was selected due to its strong experimental and modeling heritage and its straightforward interaction with the wavefront control model. To ensure relevance to current space coronagraph instruments, specifically modeling of the Roman Coronagraph Instrument (CGI), the study focused on high-order flat DMs in 48×48, 1mm pitch format. In addition to constraining performance with actuator count, the study revealed that control performance is highly sensitive to the full width at half maximum (FWHM) parameter of the PDM influence functions, with significant performance degradation observed when the FWHM approaches $2\times$ the actuator pitch, at which point actuator influence functions begin to completely overlap. This result is not particularly surprising for a continuous facesheet DM, but was valuable in guiding conversations with vendors in the survey for fabrication of the first prototypes.

2.1 Key PDM Parameters

A number of performance metrics are discussed throughout this work as key areas being simulated and tested in the development of the PDM. Note these are not comprehensive requirements of an HWO DM. The best current draft of the requirements was developed in a study run by the NASA Exoplanet Program Office[5] as a prompt for vendor technology development of the high order DMs, with the results summarized in Groff et al.[6] Many of these requirements will ultimately apply to a flight PDM, with some notable departure values such as actuator count, stroke, and pitch. The specific values would depend on the chosen control architecture, but the Gen2 device is a reasonable stand-in for what we would expect those values to be (1k actuators, 1μm stroke, 1.5mm pitch). Below is a brief list and description of the key parameters critical to designing testing with the Gen1 device.

- Influence Function - The marginal phase change incurred at the DM plane after applying a constant command size to a single actuator.

- FWHM - The influence functions of continuous facesheet DMs are typically well-described by a 2D Gaussian. The FWHM describes the characteristic size of the influence function.

- Actuator pitch - Distance between actuators. Use of DMs in industrial and defense applications have driven down manufacturing costs, but this has resulted in actuator pitch being an

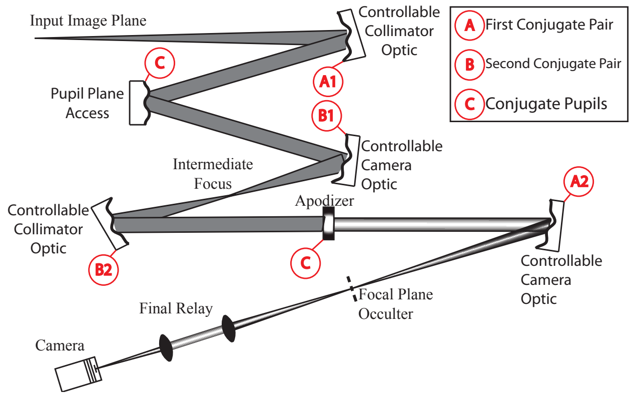

Fig 1 Notional optical configuration from initial study in Groff et al.[3]

impractical parameter to tune freely.

- Resonant frequency - For continuous facesheet DMs, this typically corresponds to the first excitation mode of the flexible membrane and actuator array.
- Settling time - The time period between receipt of a command by the controller to the completion of the actuator movement.
- Hysteresis - How much the current position of an actuator depends on that actuator's position history.

2.2 Multiple PDMs

The optical configuration in Groff et al.[3] incorporated four PDMs: three positioned before the SPC and one after. The PDMs were strategically placed such that two PDMs were optically conjugate to each other, and the other two PDMs formed a second conjugate pair, enabling coordinated wavefront control across multiple optical planes. Each PDM had a 12×12 actuator array, which seemed to be the minimally useful format for the dark zone in the study.

The simulations compared wavefront control performance under three configurations, shown in Fig. 1: (1) a baseline configuration using only the high actuator density pupil plane DM (flat

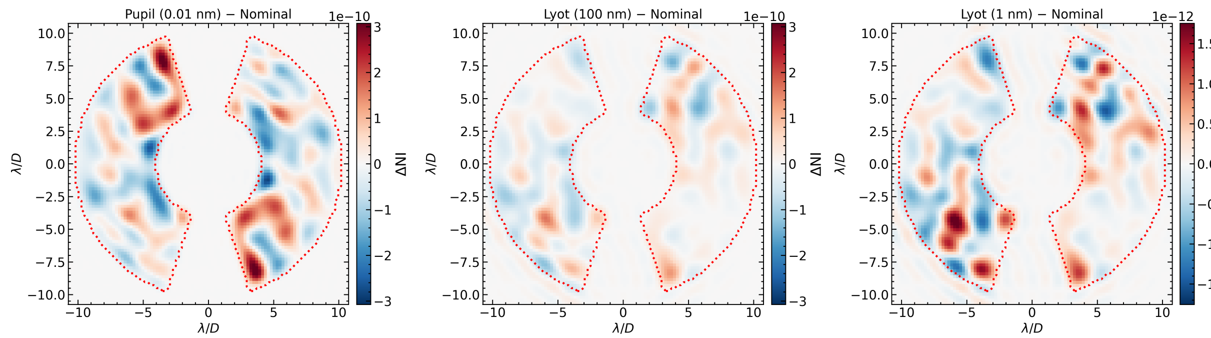

(a) (b) (c)

Fig 2 Intensity changes in the focal plane for simulated pokes of a DM actuator at pupil and Lyot planes. (a) 10 pm single-actuator poke of a DM at the input pupil plane. (b) 100 nm single-actuator poke of a DM at the Lyot plane. (c) 1 nm single-actuator poke of a DM at the Lyot plane.

DM only), 2) the pupil plane DM in conjunction with the PDMs (DM+PDMs), and (3) PDMs only without the flat DM (PDMs only). The study found that in the PDMs only configuration, removing any conjugate PDMs reduced the overall control authority, indicating that each mirror contributed meaningfully to wavefront correction. However, in the DM+PDMs configuration, the high actuator density flat DM combined with just two PDMs before the apodizer, one performing collimation and one performing focusing, was sufficient to achieve the desired contrast levels. Notably, removing the PDM located after the apodizer did not affect the final wavefront control performance. This is not a surprising result as there is less control authority left with some of the light removed, but it does raise an interesting question as to whether more stroke could be used at such a surface to relieve bit-depth requirements on the upstream DMs to achieve the deepest contrast levels.

As a simple demonstration of the concept, we go a step further from a DM post-apodizer and consider adding a DM in the Lyot plane. We simulate our testbed with its aberrations scaled down to have a $\sim 1 \times 10^{-10}$ dark hole, and add in a hypothetical DM to the Lyot plane. We then poke this Lyot plane DM and compare the image plane response to a single actuator poke of our pupil DM. As expected, we find that a 10 pm actuator poke of the pupil DM modulates the normalized intensity at the $\sim 1 \times 10^{-10}$ level, shown in Fig. 2(a), whereas we see in Fig. 2(b) that the actuator poke at the Lyot plane requires 100 nm of stroke to modulate the image at a similar intensity. As seen in Fig. 2(c), a 1 nm actuator poke at the Lyot plane changes the image intensity by $\sim 1 \times 10^{-12}$, which explicitly shows that the required control precision in the image is achievable with a coarser step size. This is quite compelling, but note that there may be additional complications with practical implementation which have not yet been studied such as potentially intrisically higher alignment or knowledge sensitivity for the control

Returning to the principal objective of the PDM modeling, the simulations demonstrate that combining PDMs with a pupil DM achieves comparable broadband contrast to two DMs in series. By leveraging the combined control authority of multiple DMs, a uniform dark hole extending to $7.5\lambda/D$ on both sides of the image plane was achieved.Three key findings emerged from these multiple DM trade-off studies: (1) the FWHM of the actuator influence function has a substantial effect on achievable contrast, (2) actuator placement relative to the coronagraph mask critically influences control authority, and (3) while increasing actuator density clearly improves contrast, the minimum number of PDM actuators required to achieve extremely high contrasts in broadband light is actually quite modest, provided that at least one high actuator density DM is located at the pupil plane. This indicates that this is a valuable instrument architecture trade compared to incorporating a second high actuator count DM far out of pupil, significantly driving instrument layout and volume. This is of particular impact because the required propagation distance scales as the square of the beam size (which is driven by actuator count and pitch).

Table 1 A brief summary of the Flat DM + PDM trade study performed in Groff et al.

Configuration	20% Contrast	Notable Changes
1 flat pupil DM	5.178×10^{-7}	Controllability baseline
[3] 4 PDMs	2.636×10^{-7}	Better performance than a lone pupil DM, indicating control authority of aberrations
1 flat DM + 4 PDMs	2.1×10^{-9}	Performance matched simulations made by Roman CGI at the time of publication[7]

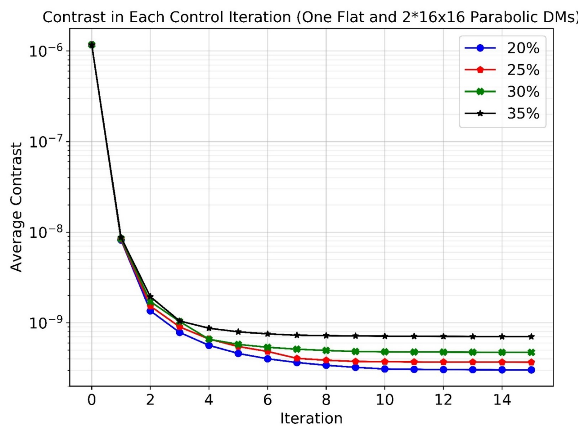

Fig 3 Contrast versus iteration for different bandwidths. Phase and amplitude aberrations were introduced at different optical planes, and the bandwidth was varied from 20% to 35% in increments of 5%. The simulations utilized two 16×16 parabolic DMs and a 32×32 BMC DM at the pupil plane.

2.3 Contrast Performance as Function of Bandwidth

Building on the original results of Groff et al.,[3] we carried out further simulations in subsequent work[8,9] to find the limits of using parabolic DMs for wavefront control. To study the performance of the parabolic DM based SPC and its sensitivity to aberrations, we developed a coronagraph model in Python utilizing both Fourier and Fresnel propagation methods. The model was validated by comparing its performance against the widely-used PROPER optical propagation library.[10] The simulation framework is capable of incorporating multiple DMs and introducing aberrations at arbitrary locations throughout the optical train, enabling comprehensive trade studies of various system configurations.

For the simulations presented in this section, we used the same SPC design from Groff et al. but increased the size of the dark hole from $4.5 - 7.5\lambda/D$ to $5 - 12\lambda/D$. Specifically, we tested parabolic DMs for broadband wavefront control and conducted design trade studies to define manufacturing requirements for a potential future device. These studies used the specifications for a Boston Micromachines Corporation (BMC) kilo-DM at the pupil plane and two PDMs.[11] One of the PDMs was used to replace a focusing off-axis-parabola (OAP) and another to replace a collimating OAP. For the PDMs, we assumed similar specifications to the DM-97 from Bertin Alpao (Grenoble, France).[12] We assumed a $f/30$ (60 inch focal length and 2 inch diameter) PDM in order to place less stringent manufacturing requirements that were deamed feasible for the first generation design. We used similar influence function FWHM characteristics of the DM-97, scaled to match the 2 inch diameter PDM with 16×16 actuators. The system was already aligned with surrogate mirrors in place of the DMs. Hence, our approach to simulating performance with a relevant aberrated field (with DMs) begins with the measured wavefront aberrations of the testbed. We then also add simulated PDM aberrations, as well as phase and amplitude aberrations of the BMC DMs based on their component-level measurements and respective locations in the testbed. Performance was evaluating with a varying bandwidth from 20% to 35% with an increment of 5%. The simulations performed electric field conjugation (EFC)[1] with perfect electric field estimate. In these simulations, we assume two 16×16 PDMs and a 32×32 BMC DM.

The result of this test is presented in Fig. 3) and Table 2. The simulations show that that the final achievable contrast, even at bandwidths as high as 35%, was $<10^{-9}$ (without relinearization of the control Jacobian matrix). Based on these promising results, we worked with Bertin Alpao (Grenoble, France) to manufacture a PDM with 277 actuators, hereafter referred to as the Gen1 PDM, which was delivered to NASA GSFC under the ExoSpec work package.[13]

Table 2 Final contrast for different bandwidths using two 16x16 parabolic DMs and one flat 32x32 pupil DM.

Bandwidth	Final Contrast
20%	3.1×10^{-10}
25%	3.9×10^{-10}
30%	4.7×10^{-10}
35%	7.1×10^{-10}

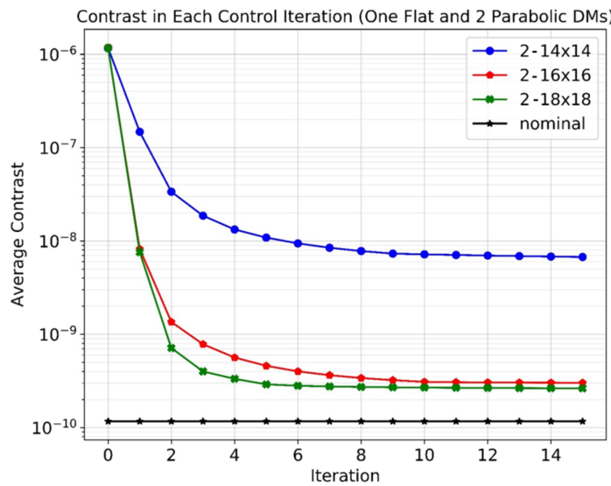

Fig 4 Contrast versus iteration for different actuator count parabolic DMs. A 32×32 pupil plane DM was used with two parabolic DMs in focusing and collimating arrangement, each with 14×14, 16×16, or 18×18 actuators. Using two 16×16 parabolic DMs improves the final contrast by more than an order of magnitude compared to the 14×14 configuration, while increasing to 18×18 actuators yields only marginal improvement. These results were obtained without control Jacobian relinearization.

2.4 Minimum Actuator Count

To determine the necessary actuator counts of the PDMs, we ran simulations with two parabolic DMs with 14×14, 16×16, and 18×18 actuators, as well as the BMC DM at the pupil plane. The simulations used 20% bandwidth light centered at 633 nm and incorporated the ripple 3 SPC. We found that using two 16×16 parabolic DMs improves the final contrast by more than an order of magnitude compared to the 14×14 case, but increasing the number of actuators to 18×18 did not offer any significant additional improvement as shown in Fig. 4.

While the long-term goal is to incorporate two parabolic DMs and two flat DMs in the optical system, the first-generation laboratory configuration utilizes a single PDM in the collimating

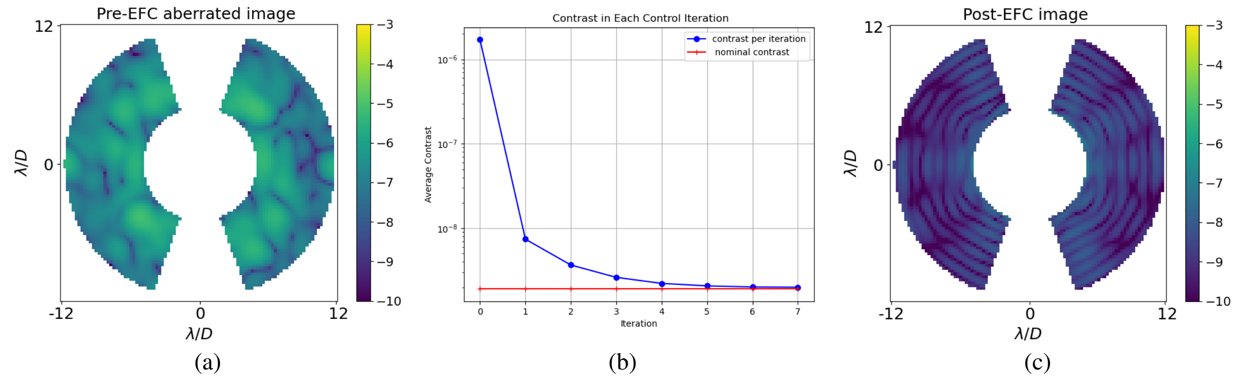

Fig 5 (a) Pre-EFC aberrated image, (b) Contrast versus iteration, and (c) Post-EFC image for the first-generation laboratory configuration using a single 16×16 collimating parabolic DM and a BMC Kilo-DM flat DM at the pupil plane. The simulation was performed with 18% bandwidth light using a shaped pupil coronagraph apodizer designed for segmented apertures similar to LUVOIR-B.

position along with one BMC kilo-DM. To validate this configuration, we performed simulations using a lab apodizer, shown in Fig. 8b. An 18% bandwidth simulation was conducted to evaluate the system's ability to achieve high-contrast dark zones with this reduced PDM configuration. The simulations results, shown in Fig. 5, shows that the EFC loop converges in 5-6 iterations.

3 Parabolic Deformable Mirror Project Development Plan

3.1 Exoplanet Spectroscopy High Contrast Testbed

The primary purpose of the Exoplanet Spectroscopy High Contrast Testbed is to verify the performance of the parabolic DM architecture within a complete coronagraph system. In addition, this testbed is also used for testing wavefront sensing and control techniques and high contrast integral field spectroscopy. One will note that we baseline a single plane apodizer, which means we are currently not testing extremely low inner working angle performance. This is by design. The primary purpose of this testbed is to test and characterize performance of the PDM, not the apodization method. It is imporant to establish baseline limitations of the PDM on the path to tackling comprehensive performance required for HWO.

The layout, shown in Fig. 6, has locations for both parabolic and two DMs in series so that the control architectures may be directly compared. Near-term, the testbed will have two BMC kilo-DMs and a single PDM. Long-term, the testbed can accommodate a second larger PDM and we intend to integrate a 97 actuator PDM that serves as a pathfinder for the Gen2 PDM fabrication, and doubles as a low order corrector. A 4D interferometer or fiber-coupled laser can be used interchangeably to serve as a starlight emulator, and the light from this source is then collimated using a large off-axis parabola (OAP). A 2-inch piezo-driven tip-tilt fast steering mirror (FSM) defines the instrument entrance pupil ahead of the coronagraph. The subsequent focusing OAP is notable as being the surrogate for the Gen1 PDM. Continuing on downstream, several more OAPs of various focal lengths are used to create multiple pupil planes across the test bed. Although not shown in Fig. 6, two of these pupil planes are currently occupied by a 32×32 actuator DM from BMC and a carbon nanotube shaped pupil apodizer. If desired, a Lyot stop can also be introduced at the final pupil plane of the system, but the baseline shaped pupil is a single plane apodizer and does not require it. At the coronagraph focal plane, the focal plane mask (FPM), which has a Zernike phase mask on the front side, directs the rejected starlight to a low-order wavefront sensing (LOWFS) camera while the desired dark zone region is reimaged onto a final science camera. Further details on the apodizer and FPM can be found in subsections 3.3 and 3.4, respectively.

Initial characterization and rough alignment of each optical element was performed with a combination of a laser tracker and theodolites. Fine alignment was then completed by operating the 4D PhaseCam interferometer in double-pass mode, in conjunction with a calibrated flat mirror or CaliBall depending on the beam state downstream of the optic under test. This process was repeated iteratively for the addition of each subsequent element in the optical chain.

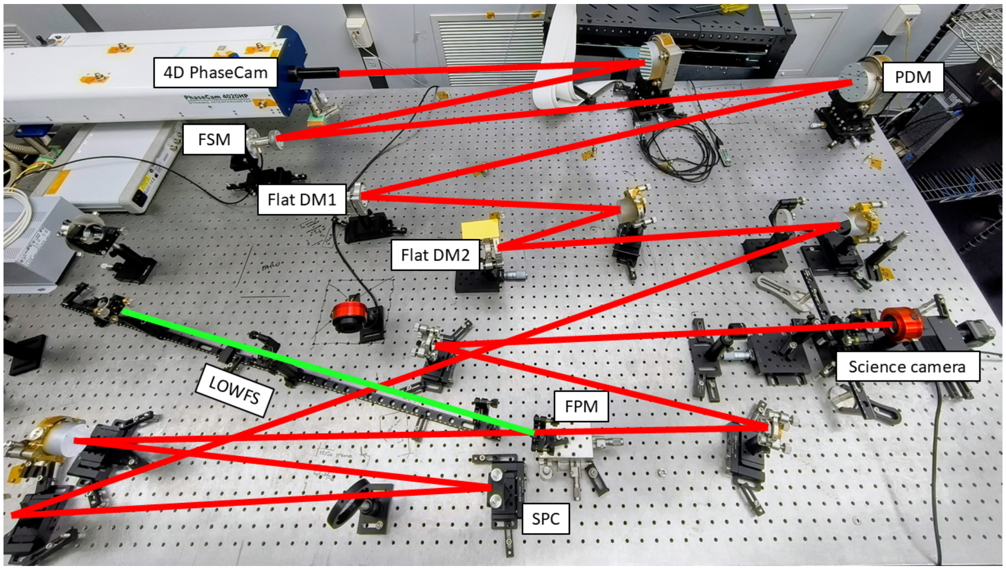

Fig 6 The Exoplanet Spectroscopy High Contrast Testbed with overlaid ray trace. In this photo, DM positions are occupied by surrogates, however the label is overlaid to indicate locations for the BMC and Bertin Alpao DMs. The 4D PhaseCam interferometer is co-aligned with a hot-swap fiber source and the final science camera is used to image the speckle field. The read raytrace follows the channel to the speckle image, and the green raytrace shows the path from the focal plane mask to the LOWFS.

3.2 Dedicated Characterization Testbed

The purpose of the characterization testbed is to verify performance of all incoming optics, both static and deformable, prior to incorporation on the Exoplanet Spectroscopy High Contrast Testbed. A Zygo interferometer is used to supply a 4 inch collimated beam centered at 632.8 nm, and can be used in conjunction with a CaliBall to perform double-pass measurements that allow us to quantify surface errors, off-axis distance, and focal length of the static OAPs. For cases where the inherent surface wavefront error is too large for a measurement to converge in the Zygo software, a collimating lens and Phasics SID4 wavefront sensor (WFS) can be utilized instead. The setup is controlled with a suite of custom Python scripts, and a layout diagram for this testbed is shown in Fig. 7.

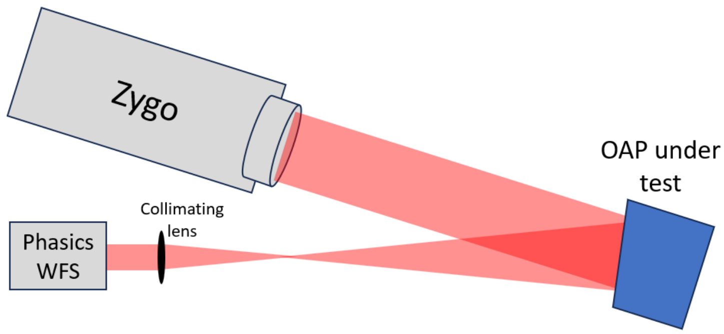

Fig 7 A top-down diagram of the characterization testbed, which includes a Zygo interferometer for double-pass interferometry that produces a 4-inch collimated beam, and a Phasics WFS for wavefront sensing in collimated space.

3.3 Apodizers

Through a collaboration with Lambda Consulting, we have produced three carbon nanotube coronagraph masks with designed average contrast of 10^{-9} over their respective dark zones (DZs). The masks have been optimized for fully unobscured, and segmented off-axis pupils. The segmented mask uses the LUVOIR B aperture since it was the most relevant representation of a large HWO aperture available at the time. The first has a DZ of $4 - 12\lambda/D$ (Fig. 8 a), the second spans $5 - 13\lambda/D$ (Fig. 8 b), and the third covers $6 - 24\lambda/D$ (Fig. 8 c). To manufacture a binary apodizer with this technique, the mirror must first be fabricated from single-crystal silicon, which is figured flat. Next, a multilayer-coating resistant to 750° C growth temperatures is applied as a reflective layer, and the apodizer pattern is laser written on the mirror coating with a resolution of several microns. After the photoresist layer on the mirror is developed, an ultra-thin layer of catalyst is applied. The residual catalyst is lifted from areas where no nanotube growth is desired, then the mirror is put in a tube furnace where carbon nanotubes are grown using a chemical vapor deposition process.

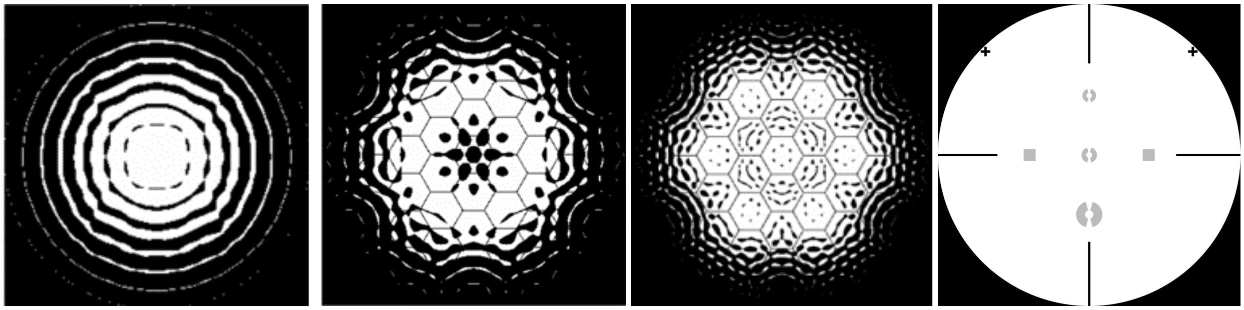

(a) (b) (c) (d)

Fig 8 Diagrams of the carbon nanotube apodizers produced for High Contrast Testbed. The circular aperture case is shown in (a), while the segmented aperture case for small and large dark zones is shown in (b) and (c), respectively. An image of the focal plane mask shown in (d).

3.4 Focal Plane Mask/Zernike Phase Mask

The FPM design is shown in (Fig. 8(d)). Each mask in the FPM has three different regions: 1) the reflective central phase disk of the FPM that has a dimple diameter of 80 microns and depth of 80 nm, 2) a reflective region outside the phase disk, and 3) the intermediary bow tie-shaped region that allows the transmission of light along the science path. The phase-shifted light from the center of the mask interferes with the rest of the light from the Point Spread Function (PSF) and is relayed to another pupil plane, which now has information about the wavefront encoded in the intensity pattern recorded by the detector. Using the intensity pattern at the detector plane, low-order aberrations are inferred and used in closed loop feedback, principally the FSM loop. This type of low-order wavefront sensor is typically referred to as a Zernike wavefront sensor.[14–16]

3.5 PISCES

The Prototype Imaging Spectrograph for Coronagraphic Exoplanet Studies (PISCES) was designed at GSFC[17] specifically to advance high-contrast imaging spectroscopy and wavefront control. Initial wavefront control demonstrations with PISCES were completed in 2017, as described in Groff et al.[18] While a new IFS is being built for higher contrast demonstrations with the Decadal

Survey Testbed 2 (DST2) at JPL/HCIT, we moved PISCES back to GSFC to be integrated onto the ExoSpec High Contrast Testbed. It is presently installed on the same optical table as the characterization testbed, described in Section 3.2, for standalone operation and upgrades. PISCES will sit on posts elevated above the main testbed to collect the beam post-focal plane masks via periscope mirrors. This will allow for the testbed to operate in either imaging or integral field spectrsocopy mode for high-contrast testing. In addition to testing control algorithms with IFS data, PISCES will provide detailed spectral performance of dark holes using the PDM or two DMs in series.

4 Design and fabrication of the Gen1 PDM

After an extensive trade study, Bertin Alpao was selected to prototype the Gen1 PDM. The top level mechanical requirements for the Gen1 PDM, such as actuator pitch and focal length, were largely driven by internal manufacturing constraints and the minimum effective actuator count modeled in Section 2.4). A core design choice for this device was that the unpowered PDM have a surface figure as close to the desired shape as possible, before any actuator commands are applied. This necessitated changes to the underlying mechanical fixtures and spring matrix layout, resulting in an architecture that diverges somewhat from Bertin Alpao's typical commercial offerings. An image of the Gen1 PDM is shown in Fig. 9, and a summary of top-level mechanical specifications is given in Table 3.

5 Characterization of the Gen1 PDM

After delivery, initial alignment of the unpowered PDM was done by first aligning a static OAP mirror of the same prescription relative to the Zygo. A CaliBall was used to establish (X,Y,Z) position of the mirror focus and optimize wavefront error (WFE) in double-pass. Following this,

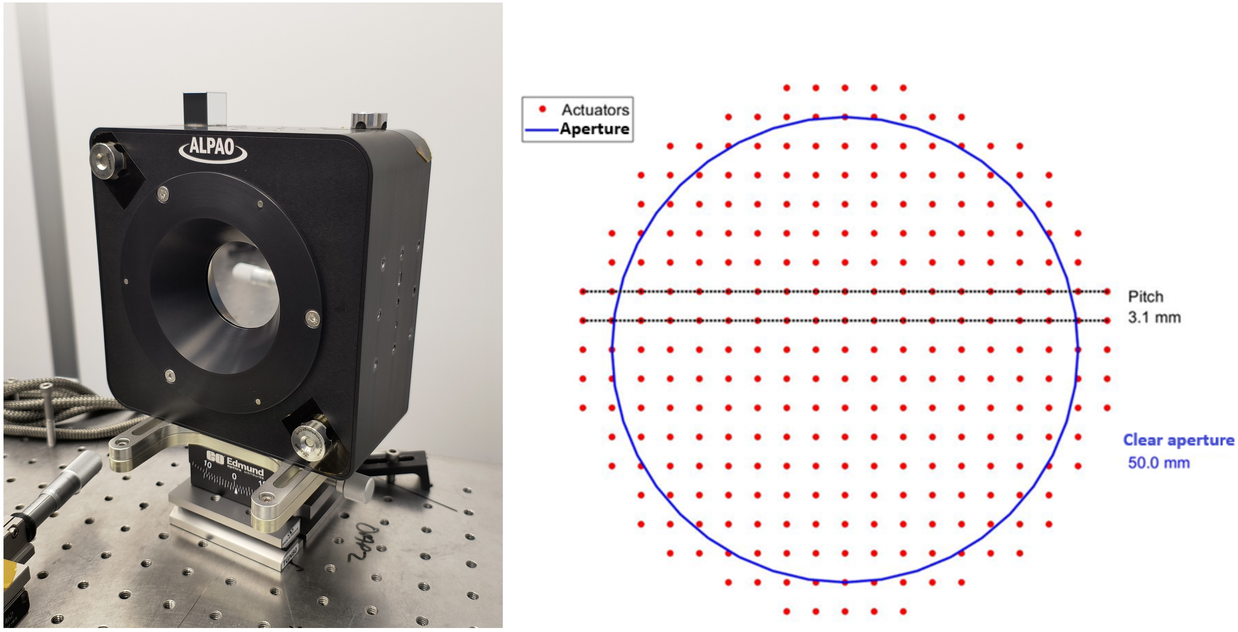

(a) (b)

Fig 9 (Left) The off-axis parabolic deformable mirror (PDM) delivered from Bertin Alpao. (Right) A diagram showing the actuator positions relative to the open aperture of the mirror surface. In this configuration, the PDMs clear aperture defines the pupil.

Metric	**Value**
Actuator pitch	3.125 mm
Actuators	277
Clear aperture	50 mm
3x3 Actuator stroke	$> 5\mu$m
Inter-actuator stroke	$> 1\mu$m
Effective focal length	1524 mm
Offset distance from center of parabola	254 mm
Resonant frequency	700 Hz
Minimum frequency at phase lag of 45°	300 Hz
Maximum settling time (at $\pm$10%)	0.55 ms
Hysteresis	<10%
Operating temperature	25° $\pm$ 5°C
Functional temperature	-5°C to 45°C

Table 3 System specifications

the static OAP was replaced with the PDM and the system was brought into rough visual alignment. Because the surface error of the unpowered PDM was too large to be measured by the Zygo software, measurements were performed in single-pass with a collimating lens and Phasics WFS instead. This configuration allows for closed-loop control of the PDM, and is the basis for the results shown in this section. A diagram of this layout is shown in Fig. 7.

5.1 Single Actuator Performance

Individual actuators are characterized by performing a series of "pokes" of various sizes and acquiring a WFE measurement at each step. The poke magnitude required by the PDM controller is a unitless parameter in the range $[-1, 1]$, which gets mapped internally to a drive current before applying said current to the actuator. Because this command mapping is not made easily accessible to the end-user, commanded poke magnitudes used throughout this work shall be reported in this unitless notation as opposed to physical units of amperage. Observable metrics of actuator performance such as displacement and range shall be reported in appropriate physical units. Note that some actuators fall outside the clear aperture of the DM, as shown in Fig. 9. While we do attempt to characterize those actuators by monitoring the mirror surface in the clear region closest to that actuator's position, this inherently results in measured ranges for those actuators being underestimated. These actuators are excluded from any statements about typical actuator performance.

The first features to be characterized were influence functions and actuator linearity, which are shown for a characteristic actuator in Fig. 10. All actuators, except one that was purposefully disconnected by the manufacturer, exhibit a similar influence function morphology and degree of linearity, and all values reported in this section were acquired with all other actuators at their unpowered positions. By performing both an up-sweep followed by an immediate down-sweep through the range of poke magnitudes we can also calculate hysteresis, which is shown alongside a plot of optical surface range in Fig. 11. Actuators clearly within the open aperture of the DM have a large range of motion, with mean (standard deviation) of 7.2 (1.2) μm, whereas the actuators closer to the perimeter are pre-tensioned to establish the desired surface curvature, and thus have a somewhat diminished range of 4-6 μm. The 14-bit driving electronics behind each actuator imply a theoretical mean actuator resolution of 0.44 nm. While observed hysteresis is larger on these high-range actuators, the thermal effects discussed later in Section 5.3 likely influence the measurement by an unclear amount. For this reason, hysteresis is not taken into account during our nominal closed-loop control algorithms.

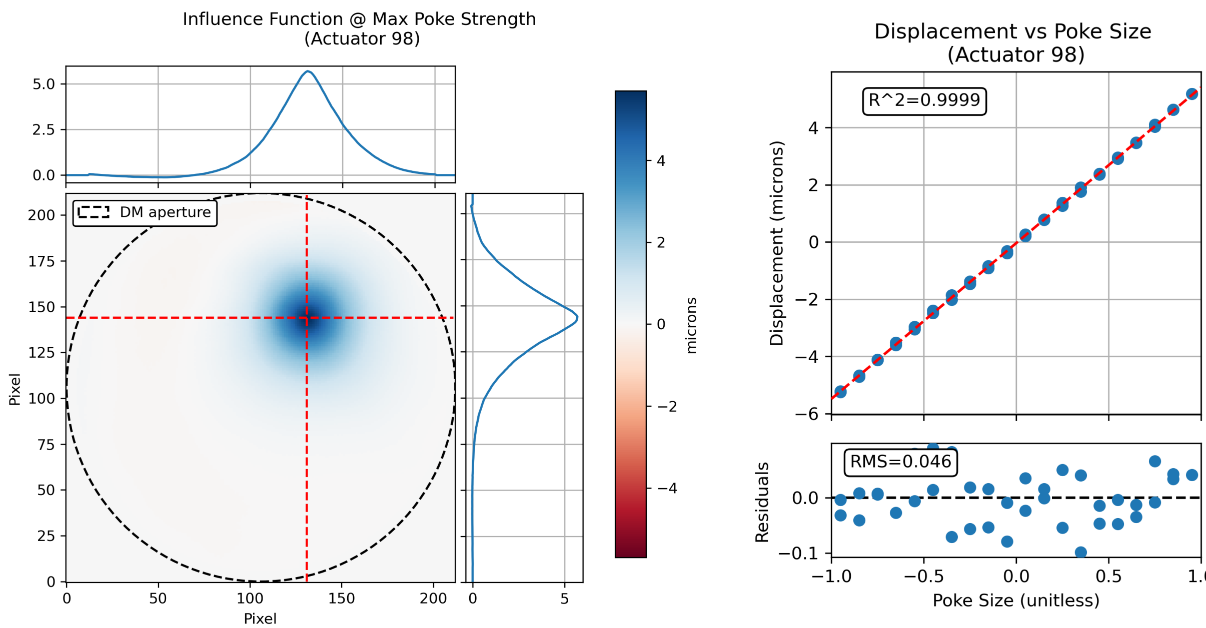

(a) (b)

Fig 10 (Left) A characteristic influence function for one actuator of the PDM. (Right) Actuator displacement in microns vs normalized poke magnitude, where the poke magnitude is a unitless parameter in the range [-1, 1] representing the maximum command range that can be applied to the actuator. This normalized range is linearly mapped to drive current by the PDM controller, with ± 1 corresponding to the maximum positive and negative actuator displacements achievable by the PDM.

5.2 Closed Loop Performance

Closed-loop control of the PDM is accomplished through singular value decomposition (SVD) of the stack of influence functions, where the first 150 SVD modes are retained for wavefront control. Because this is a prototype device that is the first of its kind, the unpowered PDM has a substantial RMS WFE of $\sim$3.5 μm, as shown in Fig. 12. However, after a few iterations, this can

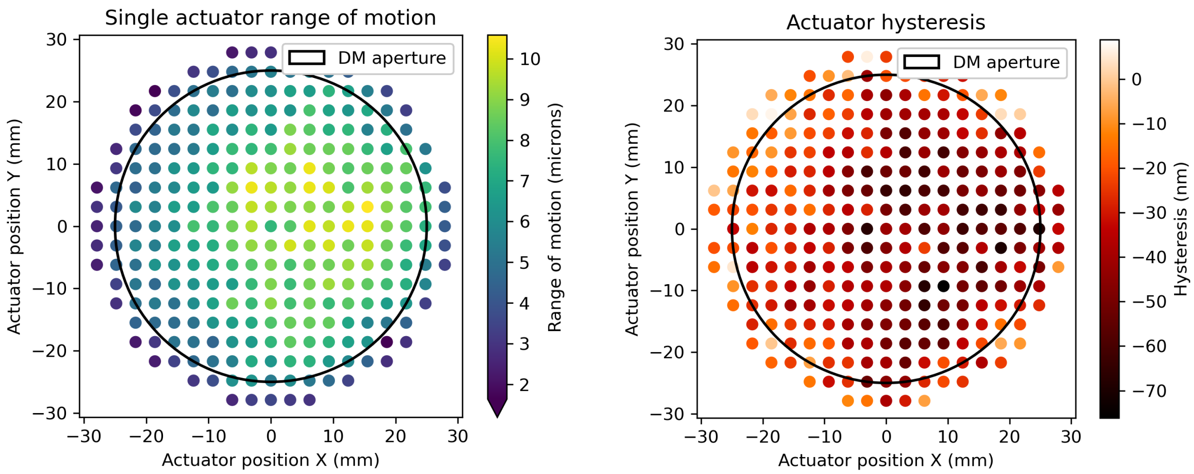

(a) (b)

Fig 11 A map of optical surface range (in microns) for individual actuators (Left) and hysteresis for each actuator (Right) when applying single-actuator pokes. While all actuators were measured, those that fall outside the DM clear aperture have inherently higher uncertainties and are likely underestimates.

be brought down to ≈170 nm, as demonstrated in Fig. 13. The actuator print-through observed in the residual WFE is only apparent after flattening the PDM to its prescribed shape. The remaining surface figure error is comprised of low-order spatial frequencies that accumulate between control iterations. To improve this stability in the next iteration of the setup, we are exploring the use of a Zernike wavefront sensor that will allow us to increase the speed of the control loop dramatically.

Actuator print-through and heat buildup are the two limiting factors for this device. Print-through limits the quality of the final optical surface, while heat dissipation limits the amount of time that this surface figure can be maintained. As shown later in Section 5.3, actuator displacement can change significantly as a function of temperature. After the WFE from the unpowered PDM is removed during the first few iterations of a closed-loop control run, the power consumption of the PDM causes its internal temperature to slowly rise. This rising temperature starts a positive feedback loop where new aberrations are introduced by the warm actuators, and more current is applied to those actuators in order to compensate. Because of this, the optimal surface figure can be

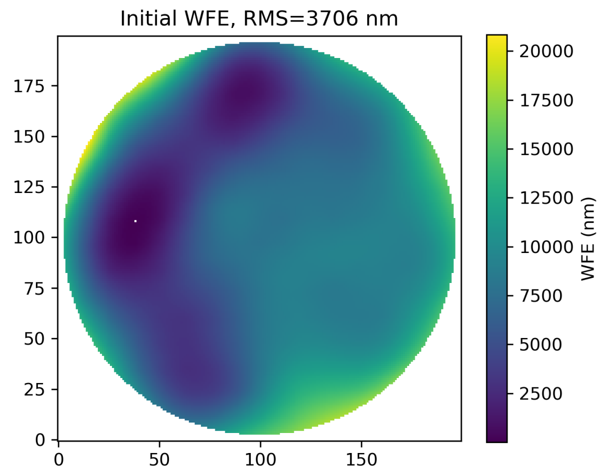

Fig 12 Initial surface figure of the full-aperture PDM.

maintained for about ∼15 minutes before a thermal runaway begins that results in the PDM being triggered to automatically return to a safe, unpowered state. This process is illustrated in Fig. 14. By incorporating a pellicle beamsplitter to monitor the downstream PSF with a high-speed camera, it is clear that the variation in the measured WFE is real and occurs on timescales faster than our control loop, which is limited by the speed of the Phasics sensor.

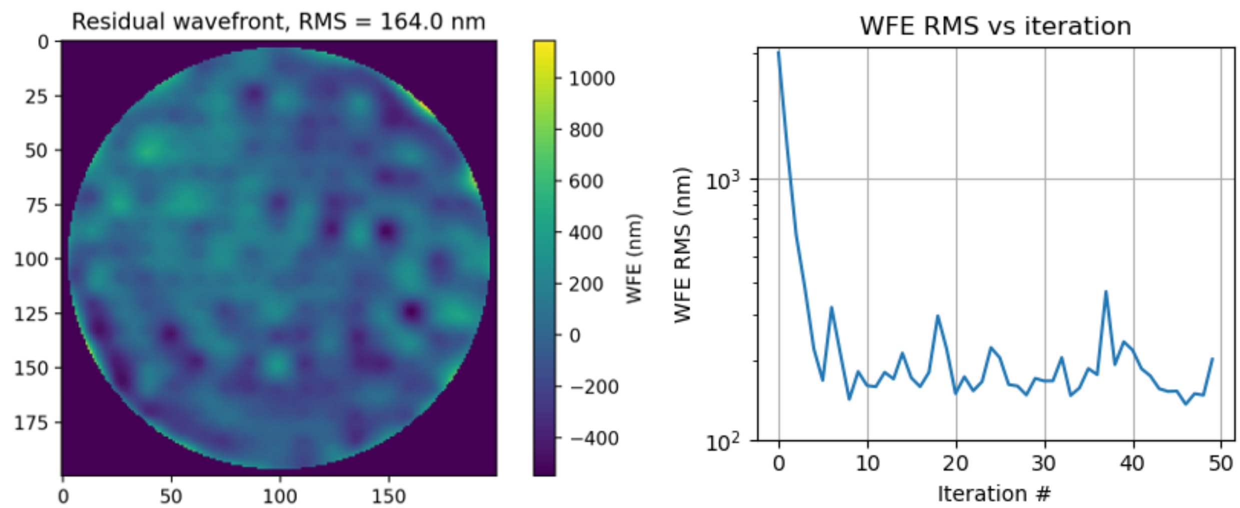

(a) (b)

Fig 13 (Left) The ultimate WFE achieved with the full-aperture PDM. Actuator print-through can be seen as a faint waffle pattern. Thermally-induced WFE seems to manifest itself as structure with a characteristic frequency of ∼several times the actuator pitch. (Right) A plot of WFE vs iteration number.

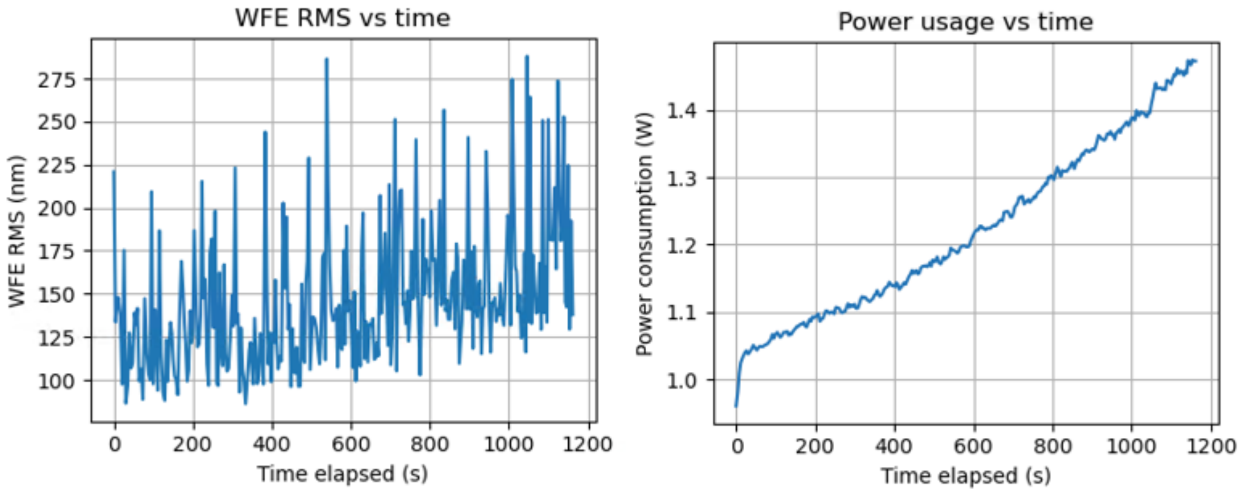

(a) (b)

Fig 14 The result of a longer closed-loop data run where the PDM started from an optimized state. Plots of WFE and power consumption are shown here on the left and right, respectively. Notice that the power consumption is slowly rising as actuator current is increased to compensate for heat-induced WFE, beginning a positive feedback loop that results in the PDM triggering a shutdown for safety.

5.3 Thermal Dependence

As mentioned in Section Sec. 5.2, the actuator displacement was found to correlate strongly with the internal temperature reported by the DM. To investigate this, a number of tests were performed to monitor the displacement of individually-poked actuators under a variety of thermal conditions. In one test, illustrated in Fig. 15, the PDM is allowed to cool down to ambient temperature before being turned on and having a normalized poke magnitude of +0.3 applied to all actuators, except Actuator 120, which received a poke with a normalized magnitude of +0.95. WFE measurements were then acquired with the Phasics WFS for 30 minutes. The Phasics WFS itself has a read noise of $\sim$several nanometers, and the control loop, which is dominated by Phasics readout time, runs at 0.25 Hz. Although the bulk mirror surface changes significantly over time, the change is most pronounced at the position of the actuator receiving the largest magnitude poke (and thus, drawing the most power). Attempts to mitigate this effect by removing the rear panel of the PDM housing to improve airflow proved relatively ineffective.

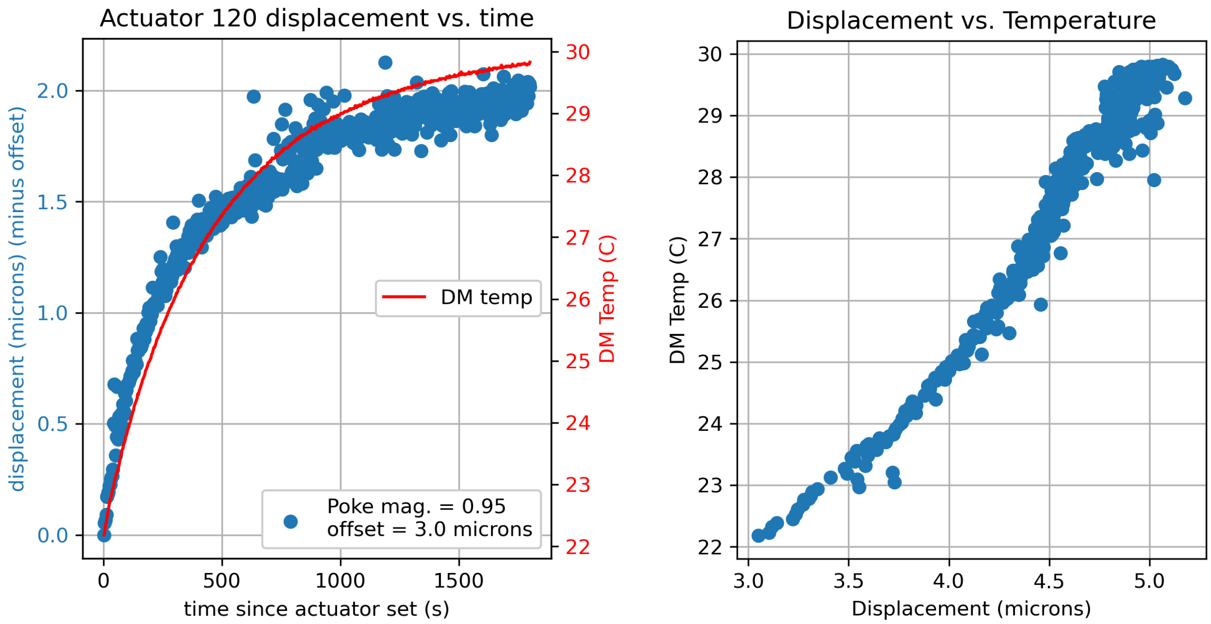

(a) (b)

Fig 15 A plot of displacement over time for a single actuator when starting the device up from cold. The surface figure of the PDM is strongly correlated with internal temperature, which is itself a byproduct of its relatively high power consumption

5.3.1 Power Consumption

One of the downsides of voice coil-type deformable mirrors is their inherently higher power consumption. Effectively shedding this heat and preventing it from influencing the surface figure (as demonstrated earlier in Section 5.3) was a key driver in our discussions with Bertin Alpao with regards to improving the Gen2 device. While the Gen2 PDM will almost certainly have a higher power consumption than the current model (due to a higher actuator count), it will also incorporate water cooling to improve temperature stability. It is worth noting here that given the extent of new engineering required for the Gen1 device, active thermal management was not incorporated to the design requirements. Based on the results here and Bertin Alpao's own development for ground observatories, active thermal management is much better understood and will be included in the Gen2 device. In production of the Gen1 prototype, Alpao utilized an experimental mount that allowed the optic to come close to the final shape in an unpowered state. The design of these actuators is also being updated to be consistent with Bertin Alpao's current model lineup, which exhibits significantly less thermal dependence and can operate for extended periods of time without overheating. For the current prototype, the correlation between equilibrium temperature, power consumption, and mean poke magnitude are shown in Fig. 16. As expected, the relationship between power consumption and equilibrium temperature is linear, while the relationship between power consumption and poke magnitude is quadratic.

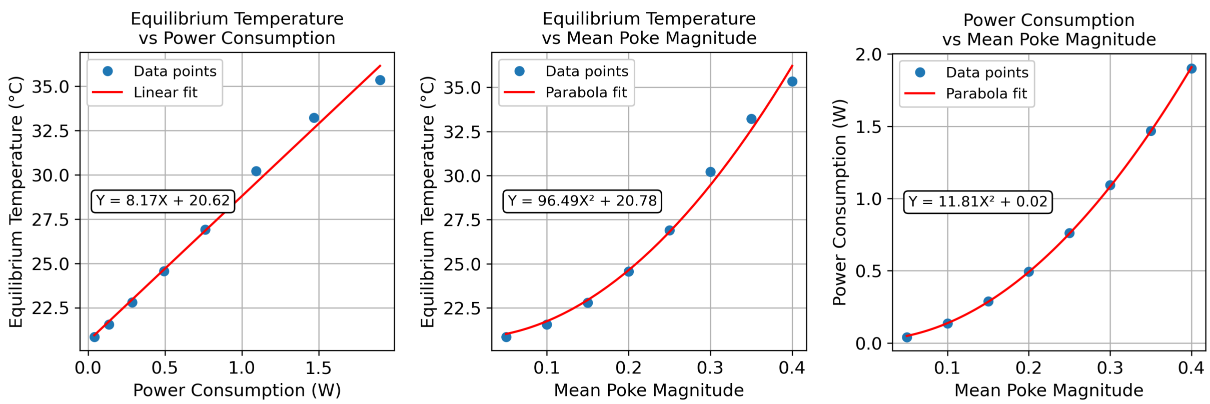

(a) (b) (c)

Fig 16 Thermal and power response of the Gen1 PDM. a) Equilibrium temperature as a function of power consumed, b) relationship between mean poke magnitude and equilibrium temperature, and c) relationship between mean poke magnitude and power consumed.

6 Gen2 PDM Development Status and Future Plans

During a preliminary review, Bertin Alpao presented findings that motivated several key design choices for the Gen2 PDM, which will have an actuator upgrade to a 32x32 array with 1.5 mm pitch. Notable factors presented during this review included, but was not limited to: expected actuator yields, spring stiffness, membrane thickness, actuator range of motion and print through, power consumption, and heat dissipation. The actuator count increase does allow for extending dark hole size, also has a couple of practical motivations. First, this fits better into the Bertin Alpao standard product line which saves in cost and complexity. Second, it must have approximately the same physical clear aperture with half the actuator pitch in order to not trigger a major redesign of the ExoSpec testbed. Following this, Bertin Alpao executed a series of modeling and pathfinder device testing.

Additionally, a series of high-fidelity models and accompanying lab measurements were produced by Bertin Alpao to study the effects of spring stiffness and membrane thickness on performance metrics like actuator range of motion and print-through. With this information, a combination of parameters that will meet project requirements was identified for use in the Gen2 device. In addition to an updated spring stiffness parameter, the voice coils have been updated to a design that exhibits very little thermal dependence. This improvement has already been validated through Bertin Alpao's extensive in-house product development, and its successful implementation across their existing commercial product line provides a high degree of confidence in addressing our thermal dependence concerns.

Lastly, several prototype spring matrices were produced to verify expected actuator yield, with results indicating an expected performance in-line with other model product lines. While a 100% yield is not practical in this case, additional modeling work will be carried out at GSFC to quantify the impact of all identified floating actuators. As part of the manufacturing process, and doubling as a risk-reduction effort, a fully-functional 97-actuator model is being produced and will be delivered to GSFC prior to completion of the 32x32 actuator device. This 97-actuator device will undergo a similar characterization campaign to the Gen1 device described in this work, which will minimize turnaround time of the Gen2 device upon receipt.

The 97-actuator PDM is highly compelling for two reasons. It will serve the ExoSpec lab in early validation of improved device performance well ahead of the 32x32 device delivery, and it affords the opportunity to test the value of a PDM as a low-order wavefront corrector. Studies of independent flat low-order correctors using Xinetics surface parallel technology are underway.[19] Since the technology may also be fabricated in a curved array, this also presents another avenue for low-order PDMs as independent correctors. Offloading large amplitude, potentially fast, low-order dynamics from the observatory from the high-order DMs used to dig dark holes is highly compelling. Testing this capability with multiple technologies is very exciting, and we leave that to future work as we begin the Gen2 device fabrication.

7 Conclusion

The successful development and characterization of this parabolic DM represents an important step toward more robust and higher-performing coronagraph instrument designs for future exoplanet imaging missions. By integrating wavefront control capabilities directly into the system's powered elements, parabolic deformable mirrors enable new system-level instrument trades that can ease design constraints associated with more traditional, high actuator count flat DMs. This approach also reduces single point of failure risks by distributing wavefront control across multiple elements, while increasing maximum control bandwidth.

The Gen1 device has proven the manufacturabiliy of a PDM and informed improvements in the Gen2 device. The Gen2 PDM incorporates changes that will improve upon the performance of the Gen1 device in nearly all metrics; particularly in thermal dependence and actuator print-through. The results presented here successfully demonstrate the core functionality of PDM concept, and indicate a clear pathway for future development improvements.

Disclosures

The authors declare no conflicts of interest.

Code and Data Availability

Not Applicable.

Acknowledgments

We would like to thank Bertin Alpao for the thoughtful contributions, engineering expertise, and responsive technical support provided throughout this collaboration. The project is supported by NASA HQ-directed ExoSpec work package under the Internal Funding Scientist Model (ISFM) and NASA GSFC Internal Research and Development (IRAD) program. The apodizers were fabricated under support from the Small Business Innovation Research (SBIR) program, Contract Number: 80NSSC24CA123.

References

1 A. Give'on, B. Kern, S. Shaklan, *et al.*, "Broadband wavefront correction algorithm for high-contrast imaging systems," *Proceedings of SPIE* **6691**, 66910A–1 – 66910A–11 (2007).

2 L. Pueyo, J. Kay, N. Kasdin, *et al.*, "Optimal dark hole generation via two deformable mirrors with stroke minimization," *Applied Optics* **48**(32), 6296–6312 (2009).

3 T. D. Groff, A. Lemmer, and A. J. Riggs, "A new deformable mirror architecture for coronagraphic instrumentation," in *Proc. SPIE*, **9904**, 990421 (2016).

4 N. J. Kasdin, R. J. Vanderbei, and R. Belikov, "Shaped pupil coronagraphy," *Comptes Rendus Physique* **8**, 312–322 (2007).

5 "DM Placeholder Requirements." https://science.nasa.gov/astrophysics/programs/exep/technology/tech-colloquium (2023).

6 T. D. Groff, D. Liu, E. Bendek, *et al.*, "Deformable mirror technology roadmap: architecting a path to TRL 5 for future exoplanet direct imaging space missions," in *Proc. SPIE*, L. E. Coyle, S. Matsuura, and M. D. Perrin, Eds., **13092** (2024).

7 J. Krist, B. Nemati, and B. Mennesson, "Numerical modeling of the proposed wfirst-afta coronagraphs and their predicted performances," *Journal of Astronomical Telescopes, Instruments, and Systems* **2**(1), 011003 (2015).

8 H. Subedi, J. Juanola-Parramon, and T. Groff, "Design and modeling of the off-axis parabolic deformable mirror laboratory," in *Proc. SPIE*, **11117**, 111171Z (2019).

9 H. B. Subedi, R. Juanola-Parramon, T. D. Groff, *et al.*, "Parabolic deformable mirror testbed for the ExoSpec project," in *Proc SPIE*, **11443**, 114431E (2021).

10 J. E. Krist, “PROPER: an optical propagation library for IDL,” in *Proc. SPIE*, *Proc. SPIE* **6675**, 66750P (2007).

11 T. G. Bifano, J. A. Perreault, P. A. Bierden, *et al.*, “Micromachined deformable mirrors for adaptive optics,” in *International Symposium on Optical Science and Technology*, 10–13, International Society for Optics and Photonics (2002).

12 Bertin Alpao, “Deformable mirrors.” https://www.alpao.com/products-and-services/deformable-mirrors/ (2025).

13 N. T. Zimmerman, M. W. McElwain, T. D. Groff, *et al.*, “ExoSpec project: an exoplanet spectroscopy technology research collaboration based at NASA’s Goddard Space Flight Center and Ames Research Center,” in *Proc SPIE*, **11443**, 114433T (2020).

14 F. Shi, K. Balasubramanian, R. Hein, *et al.*, “Low-order wavefront sensing and control for WFIRST-AFTA coronagraph,” *Journal of Astronomical Telescopes, Instruments, and Systems* **2**, 011021 (2016).

15 M. N’Diaye, K. Dohlen, T. Fusco, *et al.*, “Calibration of quasi-static aberrations in exoplanet direct-imaging instruments with a Zernike phase-mask sensor,” *AAP* **555**, A94 (2013).

16 R. H. Dicke, “Phase-contrast detection of telescope seeing errors and their correction,” *APJ* **198**, 605–615 (1975).

17 P. Saxena, M. Rizzo, C. Prada, *et al.*, “Commissioning and performance results of the wfirst/pisces integral field spectrograph,” in *Proc. SPIE*, **10400**, 104001P (2017).

18 T. Groff, C. Mejia-Prada, E. Cady, *et al.*, “Wavefront control methods for high-contrast integral field spectroscopy,” in *Proc. SPIE*, **10400**, 10400Q (2017).

19 J. Trauger, J. K. Wallace, J. Krist, *et al.*, "A hardware implementation for low-order wavefront sensing and control in exoplanet imaging," in *Space Telescopes and Instrumentation 2024: Optical, Infrared, and Millimeter Wave*, L. E. Coyle, S. Matsuura, and M. D. Perrin, Eds., **13092**, 130926C, International Society for Optics and Photonics, SPIE (2024).

Tyler D. Groff received his bachelor's degree in mechanical engineering and astrophysics in 2007 from Tufts University and his PhD in mechanical and aerospace engineering from Princeton University in 2012. His research focuses on visible and near-infrared instrumentation for exoplanet science, coronagraph design, and wavefront control. He is the lead engineer at Goddard for the *Roman* CGI prism and polarizer modes, the optical verification lead for the *Roman* WFI instrument, and the principal investigator for the parabolic deformable mirror and CHARIS IFS at Subaru telescope.

Hari B. Subedi is an optical engineer at NASA Goddard Space Flight Center in Greenbelt, Maryland. He received his bachelor's degree in aerospace engineering from the University of Arizona in 2013 and his PhD in mechanical and aerospace engineering from Princeton University in 2018. During his graduate studies, Hari was an NSF Graduate Research Fellow. His research interests include low-order wavefront sensing and control, deformable mirrors, and instrumentation for space-based telescopes.

Evan Bray acquired his BS in physics from Purdue University in 2015 and his MS and PhD in astronomy and astrophysics from The Pennsylvania State University in 2019. His research background is in imaging detector characterization and VIS/NIR instrumentation for astronomical telescopes. His most latest work covers the imaging and spectral verification activities for the Wide

Field and Coronagraph Instruments of the *Nancy Grace Roman Space Telescope*.

Guangjun Gao is an optical engineer at NASA, Goddard Space Flight Center (GSFC). He received his PhD in 2005 in optical engineering and instruments. He is currently involved in Roman Space Telescope (RST), Habitable World Observatory (HWO), and a Lidar project. He has more than 15 years of experience in optical design, simulation and analysis.

Neil T. Zimmerman is the Coronagraph Scientist for the *Roman Space Telescope* Project Science team at NASA's Goddard Space Flight Center. He researches techniques for directly imaging exoplanets, and supports the development of new missions through laboratory instrument demonstrations and investigations on data simulation, calibration, post-processing, and inference. He received his Ph.D. in astronomy from Columbia University in 2011, and joined the research staff of the GSFC Exoplanets and Stellar Astrophysics Laboratory in 2017.

Michael W. McElwain is the James Webb Space Telescope's Observatory Project Scientist, Habitable Worlds Observatory's Observatory Scientist, and the Exoplanets and Stellar Astrophysics Laboratory Chief at NASA's Goddard Space Flight Center. Michael's research interests include large space telescopes and specialized instrumentation for exoplanet characterization. He earned his PhD at the University of California, Los Angeles, where he was a member of the Infrared Laboratory. He was a postdoctoral researcher at Princeton University and policy fellow at the National Academies before joining NASA.

List of Figures

2 Intensity changes in the focal plane for simulated pokes of a DM actuator at pupil and Lyot planes. (a) 10 pm single-actuator poke of a DM at the input pupil plane. (b) 100 nm single-actuator poke of a DM at the Lyot plane. (c) 1 nm single-actuator poke of a DM at the Lyot plane.

3 Contrast versus iteration for different bandwidths. Phase and amplitude aberrations were introduced at different optical planes, and the bandwidth was varied from 20% to 35% in increments of 5%. The simulations utilized two 16×16 parabolic DMs and a 32×32 BMC DM at the pupil plane.

4 Contrast versus iteration for different actuator count parabolic DMs. A 32×32 pupil plane DM was used with two parabolic DMs in focusing and collimating arrangement, each with 14×14, 16×16, or 18×18 actuators. Using two 16×16 parabolic DMs improves the final contrast by more than an order of magnitude compared to the 14×14 configuration, while increasing to 18×18 actuators yields only marginal improvement. These results were obtained without control Jacobian relinearization.

5 (a) Pre-EFC aberrated image, (b) Contrast versus iteration, and (c) Post-EFC image for the first-generation laboratory configuration using a single 16×16 collimating parabolic DM and a BMC Kilo-DM flat DM at the pupil plane. The simulation was performed with 18% bandwidth light using a shaped pupil coronagraph apodizer designed for segmented apertures similar to LUVOIR-B.

6 The Exoplanet Spectroscopy High Contrast Testbed with overlaid ray trace. In this photo, DM positions are occupied by surrogates, however the label is overlaid to indicate locations for the BMC and Bertin Alpao DMs. The 4D PhaseCam interferometer is co-aligned with a hot-swap fiber source and the final science camera is used to image the speckle field. The read raytrace follows the channel to the speckle image, and the green raytrace shows the path from the focal plane mask to the LOWFS.

7 A top-down diagram of the characterization testbed, which includes a Zygo interferometer for double-pass interferometry that produces a 4-inch collimated beam, and a Phasics WFS for wavefront sensing in collimated space.

8 Diagrams of the carbon nanotube apodizers produced for High Contrast Testbed. The circular aperture case is shown in (a), while the segmented aperture case for small and large dark zones is shown in (b) and (c), respectively. An image of the focal plane mask shown in (d).

9 (Left) The off-axis parabolic deformable mirror (PDM) delivered from Bertin Alpao. (Right) A diagram showing the actuator positions relative to the open aperture of the mirror surface. In this configuration, the PDMs clear aperture defines the pupil.

10 (Left) A characteristic influence function for one actuator of the PDM. (Right) Actuator displacement in microns vs normalized poke magnitude, where the poke magnitude is a unitless parameter in the range [-1, 1] representing the maximum command range that can be applied to the actuator. This normalized range is linearly mapped to drive current by the PDM controller, with ± 1 corresponding to the maximum positive and negative actuator displacements achievable by the PDM.

11 A map of optical surface range (in microns) for individual actuators (Left) and hysteresis for each actuator (Right) when applying single-actuator pokes. While all actuators were measured, those that fall outside the DM clear aperture have inherently higher uncertainties and are likely underestimates.

12 Initial surface figure of the full-aperture PDM.

13 (Left) The ultimate WFE achieved with the full-aperture PDM. Actuator print-through can be seen as a faint waffle pattern. Thermally-induced WFE seems to manifest itself as structure with a characteristic frequency of $\sim$several times the actuator pitch. (Right) A plot of WFE vs iteration number.

14 The result of a longer closed-loop data run where the PDM started from an optimized state. Plots of WFE and power consumption are shown here on the left and right, respectively. Notice that the power consumption is slowly rising as actuator current is increased to compensate for heat-induced WFE, beginning a positive feedback loop that results in the PDM triggering a shutdown for safety.

15 A plot of displacement over time for a single actuator when starting the device up from cold. The surface figure of the PDM is strongly correlated with internal temperature, which is itself a byproduct of its relatively high power consumption

List of Tables